

## Large thermal hysteresis in a single-phase NiTiNb shape memory alloy

Genfa Kang <sup>a</sup>, Hui Zhang <sup>a</sup>, Zhiyuan Ma <sup>a</sup>, Yang Ren <sup>b</sup>, Lishan Cui <sup>a,\*</sup>, Kaiyuan Yu <sup>a,\*</sup>

<sup>a</sup> Department of Materials Science and Engineering, China University of Petroleum-Beijing, Changping, Beijing, 102249, China

<sup>b</sup> Department of Physics, City University of Hong Kong, Kowloon, Hong Kong, China

\* Corresponding authors. Email: [lscui@cup.edu.cn](mailto:lscui@cup.edu.cn) (L. Cui); [kyyu@cup.edu.cn](mailto:kyyu@cup.edu.cn) (K. Yu).

### Abstract

Large thermal hysteresis ( $T_{\text{hys}}$ ) is favorable in shape memory alloys (SMAs) because it renders wide service and storage temperature range of the SMA-made parts. In this letter, we show that large intrinsic  $T_{\text{hys}}$  up to 100K is achieved in a low Nb content (2 at. %),  $\beta$ -Nb-free and single-phase NiTiNb SMA fabricated by casting, forging, wire-drawing and annealing. Such a large  $T_{\text{hys}}$  is comparable to that of the widely used dual-phase NiTiNb SMAs in which high Nb content and  $\beta$ -Nb are required. By exploiting the grain-size-dependence of  $T_{\text{hys}}$  in our single-phase NiTiNb SMA and that in an equiatomic NiTi SMA, we attribute the large  $T_{\text{hys}}$  to the enhanced kinetic resistance of transformation by the small grains. The connection between the  $T_{\text{hys}}$  and the kinetic resistance is demonstrated by a modified dislocation-based kinetic model.

*Keywords:* NiTiNb; Single phase; Thermal hysteresis; Martensitic transformation kinetic; Shape memory alloy

Large thermal hysteresis ( $T_{\text{hys}}$ ), intrinsic or deformation-induced, is one of the most important properties of shape memory alloys (SMAs) that are used to make tube couplings or mechanical fasteners [1–3]. On one hand, larger  $T_{\text{hys}}$  usually means wider service temperature range. On the other, it permits the storage and mounting of parts at higher temperatures (especially at room temperature) and hence significantly lowers the cost [1–3]. One type of SMAs with large  $T_{\text{hys}}$  is the dual-phase NiTiNb alloys, wherein  $\beta$ -Nb phase is distributed uniformly in the NiTi matrix to confine the martensitic transformation (MT) [1,4–6]. The intrinsic  $T_{\text{hys}}$  of dual-phase NiTiNb alloys is up to 110K, and the  $T_{\text{hys}}$  becomes even larger after deformation [3,5,7]. For this reason, these alloys have been commercialized and widely used. One remained issue is that Nb possesses larger specific weight and is more expensive than Ni and Ti [8]. It is therefore of interest to develop NiTiNb SMAs with low Nb content [3,8]. However, decreasing the Nb content leads to the significant volume reduction or even the absence of  $\beta$ -Nb (single-phase) and hence the significant decrease of the  $T_{\text{hys}}$  [3,4,7,8]. It is so far challenging to develop single-phase NiTiNb alloys with comparably large  $T_{\text{hys}}$  to the dual-phase ones.

In this paper, we show that large intrinsic  $T_{\text{hys}}$  up to 100K can be achieved in single-phase NiTiNb SMAs. The alloys of different grain sizes are fabricated by induction casting, forging, wire-drawing and annealing. Such a  $T_{\text{hys}}$  value is comparable with the dual-phase NiTiNb SMAs. The thermally-induced MT behavior of the single-phase NiTiNb alloys is systematically investigated by calorimetric, electrical and synchrotron XRD methods, and compared with that of a single-phase Ni<sub>50</sub>Ti<sub>50</sub> alloy. A dislocation-based kinetic model is modified to interpret the underlying physics of the large  $T_{\text{hys}}$ .

Alloy ingots of 15 kg in weight with nominal compositions of Ni<sub>50.5</sub>Ti<sub>47.5</sub>Nb<sub>2</sub> and

Ni<sub>50</sub>Ti<sub>50</sub> (at. %) were prepared by vacuum induction melting. The raw materials used were Ni (99.96 wt. %), Ti (99.90 wt. %) and Nb (99.99 wt. %). The ingots were hot-forged at 1123K into rods of 16 mm in diameter and further hot-drawn at 1023K into wires of 0.6 mm in diameter. The hot-drawn wires were annealed at 1023K for 5 minutes and then cold-drawn via multiple steps into thinner wires of 0.26 mm in diameter at room temperature without intermediate annealing. Cold-drawing leads to amorphization of the alloy wires and subsequent annealing results in equiaxed grains [9–11]. Specimens used in this study were clip-cut from the cold-drawn wires and annealed at temperatures ranging from 673K to 1023K for 20 minutes followed by air cooling.

Microstructure was examined using a JEM-2100 transmission electron microscope (TEM) at an accelerating voltage of 200 kV and an OLYMPUS DSX510 optical microscope (OM). TEM specimens were mechanically ground and polished, followed by low-angle ion milling using a Gatan Model 691 Precision Ion Polishing System. OM specimens were mechanically ground and polished, followed by etching in solution of HF:HNO<sub>3</sub>:H<sub>2</sub>O at 1:4:5 by volume. Thermally-induced MT behavior of the specimens was characterized by using a NETZSCH 214 differential scanning calorimeter (DSC) and an electrical resistivity (ER) instrument equipped with a Keithley 2000 four-point probe system. The cooling and heating rates of DSC and ER measurements were 10K/min, and ER test was carried out at a constant current of 100 mA. *In-situ* synchrotron high-energy X-ray diffraction (HE-XRD) measurements were performed during cooling and heating at the 11-ID-C beamline of the Advanced Photon Source at Argonne National Laboratory. High-energy X-rays with wavelength of 0.1173 Å and beam size of 0.5 mm × 0.5 mm were used to obtain two-dimensional (2D) diffraction patterns in the transmission geometry using a Perkin-

Elmer large area detector placed downstream at 1800 mm away from the sample. One-dimensional (1D) XRD spectrums were generated by analyzing 2D diffraction patterns using the FIT 2D software and diffraction peaks were fitted by Gauss function.

Fig. 1 presents the microstructure of the  $\text{Ni}_{50.5}\text{Ti}_{47.5}\text{Nb}_2$  alloy annealed at different temperatures. Fig. 1a, c, e, g, i and j show the microscopy images of the longitudinal section of the specimens annealed at 673K, 723K, 793K, 823K, 873K and 1023K, respectively. Equiaxed grains were observed in all specimens. Fig. 1b, d, f, h, and k display the corresponding grain size statistics, manifesting the average grain size of 20 nm, 31 nm, 110 nm, 290 nm and 9.1  $\mu\text{m}$ , respectively. The average grain size of each specimen was determined by measuring about 200 individual grains. The average grain size of  $\text{Ni}_{50.5}\text{Ti}_{47.5}\text{Nb}_2$  specimen annealed at 873K was determined to be 710 nm by measuring about 50 individual grains. Fig. 1l shows the average grain size as a function of annealing temperature.

Fig. 2 presents the thermally-induced MT behavior of the  $\text{Ni}_{50.5}\text{Ti}_{47.5}\text{Nb}_2$  alloy. Fig. 2a shows the DSC curves during cooling and heating within 105-360K. The starting, peak and finishing temperatures of forward MT are marked by  $M_s$ ,  $M_p$  and  $M_f$ , respectively, and those of backward MT are marked by  $A_s$ ,  $A_p$  and  $A_f$ , respectively. With decreasing annealing temperature, the position and shape of the peaks vary significantly, as shown by the peak position shifting towards lower temperatures, peak area shrinkage and peak width broadening. This is because that MT is increasingly inhibited by smaller sized grains [12–14]. MT was not observed for the specimens annealed below 783K for the same reason [12–14].

Fig. 2b shows the normalized ER curves during cooling and heating within 83-623K. Inset shows an example of labeling the MT critical temperatures. For

specimens annealed below 783K, ER curves are non-hysteretic. They firstly decrease linearly down to  $T_p$ , then decrease nonlinearly to a minimum value (at ~450K), and finally increase gradually during cooling, which coincide with those during heating. This implies that MT did not occur during cooling and is consistent with DSC results. The regime between  $T_p$  and  $M_s$  is known as the precursor stage of MT [15–20] and thereby the subscript 'p' stands for precursor. For specimens annealed above 783K, ER curves are hysteretic. During cooling, they initially overlap with those annealed below 783K and then deflect at  $M_s$  towards  $M_f$ . During heating, the first deflection point is  $A_s$  and the second is  $A_f$ . It was found that  $T_p$  is nearly independent on annealing temperature, while  $M_s$ ,  $M_f$ ,  $A_s$  and  $A_f$  decrease monotonically with decreasing annealing temperature.

Fig. 2c depicts the HE-XRD patterns over 360° azimuthal angle of specimen annealed at 823K at different temperatures. It can be seen that the average structure of the specimen is B2 during cooling from 373K to 190K, as indicated by the blue curves at the bottom. Completely reversible B2↔B19' MT is revealed during further cooling to 103K and subsequent heating back to 373K. Such a temperature range is nearly consistent to those measured by DSC and ER (cyan curves in Fig. 2a-b). Therefore, in what follows  $T_{hys}$  will be calculated based on DSC and ER results.

Fig. 2d summarizes the variation of  $T_{hys}$  as a function of annealing temperature. Different methods were used for  $T_{hys}$  calculated for comparison. By using DSC results,  $T_{hys}$  was calculated by  $A_f-M_s$ ,  $A_s-M_f$  and  $A_p-M_p$ . By using ER results,  $T_{hys}$  was calculated by  $A_f-M_s$ ,  $A_s-M_f$  and  $(A_s+A_f-M_s-M_f)/2$ . Note that  $(A_s+A_f-M_s-M_f)/2$  from ER is presumably equivalent to  $A_p-M_p$  from DSC. As shown in Fig. 2d,  $T_{hys}$  calculated by different methods match fairly well and share the same varying trend with annealing temperature. As the annealing temperature decreases,  $T_{hys}$  grows

monotonically from 45K to 100K.

Fig. 2e compares intrinsic  $T_{\text{hys}}$  of our  $\text{Ni}_{50.5}\text{Ti}_{47.5}\text{Nb}_2$  specimens with those in various NiTi-based SMAs in literature, including coarse-grained near-equiatomic NiTi [21], NiTiFe (3/4 at. % Fe) [15,18,19,22–24] and dual-phase NiTiNb (3-20 at.% Nb) [3–5,7,8,25–29]. Note that  $T_{\text{hys}}$  collected are the intrinsic values but not the deformation-induced values.  $T_{\text{hys}}$  data points for near-equiatomic NiTi and NiTiNb are all associated with  $\text{B2} \leftrightarrow \text{B19}'$  MT while those for NiTiFe include two sets of data due to different MT paths. The bottom ones for NiTiFe are from  $\text{B2} \leftrightarrow \text{R}$  MT while the top ones are from  $\text{R} \leftrightarrow \text{B19}'$  MT [15,18,19,22–24]. The maximum  $T_{\text{hys}}$  (100K) of our single-phase  $\text{Ni}_{50.5}\text{Ti}_{47.5}\text{Nb}_2$  alloy is comparable to that of the dual-phase NiTiNb alloys [3–5,7,8,25–29] and is 2-3 times of that of near-equiatomic NiTi alloys [21].

To understand the underlying physics of the large  $T_{\text{hys}}$ , we need first to explore why  $T_{\text{hys}}$  of our  $\text{Ni}_{50.5}\text{Ti}_{47.5}\text{Nb}_2$  shows a strong relationship with annealing temperature (*i.e.* grain size). Fig. 3 shows the MT behavior of a  $\text{Ni}_{50}\text{Ti}_{50}$  alloy annealed at 773-1023K. Fig. 3a-c was gained by repeating the experimental procedure of Fig. 2. It can be seen from Fig. 3c that  $T_{\text{hys}}$  is not large (32K in average) and is nearly independent of grain size (annealing temperature). A clear picture of the sharp difference in the grain-size-dependence of the two systems can be found in Fig. 3d. In what follows, we attempt to discuss the origin of the sharp difference, which eventually leads to an understanding of the large  $T_{\text{hys}}$ .

The overall  $T_{\text{hys}}$  of a thermoelastic MT has two major contributing parts [30]. The first is the athermal part which related to the lattice compatibility at the austenite/martensite interface. Low lattice compatibility leads to enhanced  $T_{\text{hys}}$  [31–33]. This part of  $T_{\text{hys}}$  is determined by the middle eigenvalue of the transformation

stretch matrix [31–33] such that it in principle does not vary with grain size (see Ni<sub>50</sub>Ti<sub>50</sub> data in Fig. 3d). The second is the thermal part which is mainly related to the thermally-activated interfacial friction and typically manifests the kinetic resistance of MT [30,34–37]. The stronger the kinetic resistance is, the larger the  $T_{\text{hys}}$ .

In the present study,  $T_{\text{hys}}$  of Ni<sub>50.5</sub>Ti<sub>47.5</sub>Nb<sub>2</sub> is dictated by the second contributing part because the evident kinetic resistance of MT has been observed. As shown in Fig. 3e, ER curve of Ni<sub>50.5</sub>Ti<sub>47.5</sub>Nb<sub>2</sub> is an upward facing parabola from  $T_p$  to  $M_s$  while no average structure change is observed during this regime (Fig. 2c). This phenomenon has been widely reported in a variety of doped NiTi-based SMAs, such as Ni-rich NiTi [17,20] or NiTiFe [18,19] alloys, and is known as the precursor of MT [15–20]. The physical origin of MT precursor is still under debate [15–20,38–41]. One prevailing opinion is that it is related to the strong kinetic resistance of MT due to doped defects [17,19,20,38,41] or grain boundaries [13,14]. It has been suggested that MT tends to occur thermodynamically but is kinetically arrested [19,20,38,39,41]. The strength of the kinetic resistance is suggested to increase with decreasing temperatures [34–37], increasing concentration of defects [19,20] and decreasing grain size [13,14]. In contrast, ER of Ni<sub>50</sub>Ti<sub>50</sub> decreases linearly above  $M_s$ , exhibiting a normal metallic behavior [20]. This is also the case for all Ni<sub>50</sub>Ti<sub>50</sub> specimens annealed at different temperatures.

Furthermore, the kinetic resistance of MT can also be unveiled by looking into the equilibrium temperature  $T_0$ . By calculating  $T_0$  using  $(M_s+A_f)/2$  [21,42,43], we find that  $T_0$  in Ni<sub>50</sub>Ti<sub>50</sub> is nearly constant (Fig. 3a). This means that the MT in Ni<sub>50</sub>Ti<sub>50</sub> can be described by equilibrium thermodynamics and the kinetic resistance is nearly absent. In contrast,  $T_0$  of Ni<sub>50.5</sub>Ti<sub>47.5</sub>Nb<sub>2</sub> decreases drastically with decreasing grain size (Fig. 2a). These results all indicate the much stronger kinetic resistance of MT in

$\text{Ni}_{50.5}\text{Ti}_{47.5}\text{Nb}_2$  alloys than in  $\text{Ni}_{50}\text{Ti}_{50}$ .

The difference in kinetic resistance leads to the difference in the grain-size-dependence of the two alloys. For  $\text{Ni}_{50}\text{Ti}_{50}$ , the kinetic resistance is negligible as indicated by the ER trend above  $M_s$  (Fig. 3e). As a result, decreasing grain size does not cause observable kinetic resistance to MT and  $T_{\text{hys}}$  is thereby grain-size-independent. In contrast, the kinetic resistance in  $\text{Ni}_{50.5}\text{Ti}_{47.5}\text{Nb}_2$  is already strong at coarse grain sizes (*e.g.* 1023K annealing temperature). This is probably due to the excess Ni or Nb atoms with respect to  $\text{Ni}_{50}\text{Ti}_{50}$  [20,44]. With decreasing grain size, the grain boundaries pose additional constraint to MT and the kinetic resistance strengthens [13,14]. As a result, the grain-size-dependence of our  $\text{Ni}_{50.5}\text{Ti}_{47.5}\text{Nb}_2$  is strong.

By now, we have shown that the smaller grain size enhances the kinetic resistance (lowering  $M_s$  and  $T_0$ , Fig. 2a). We next show by a modified model that the enhanced kinetic resistance subsequently causes larger  $T_{\text{hys}}$ . In Ni-rich NiTi [34,35], NiTiCu [36] and NiCoMnIn [37] alloys, a dislocation-based kinetic model has been proposed to describe the enhanced kinetic resistance of the stress-induced MT in the alloys at low temperatures. In these studies, half of the stress hysteresis ( $\sigma_{\text{hys}}$ ) in stress-induced MT was considered to be analogous to the critical resolved shear stress in plastic deformation, and an equation was proposed to describe the kinetic resistance of phase boundary migration:

$$\frac{\sigma_{\text{hys}}(T)}{2} = \sigma_{\mu} + \sigma_{\text{TA}}(0) \left\{ 1 - \left( \frac{T}{T_{\text{TA}}} \right)^{1/q} \right\}^{1/p} \quad (1)$$

where  $\sigma_{\text{TA}}$  and  $\sigma_{\mu}$  are stresses corresponding to the thermal and athermal terms, respectively. The values of  $p$  and  $q$  are fitting parameters related to the shape of energy barrier against migration of phase boundary.  $T_{\text{TA}}$  is the critical temperature at

which the contribution of thermal activation term arises.

Based on equation (1), the following equation is proposed to link the kinetic resistance of the thermally-induced MT with  $T_{\text{hys}}$ :

$$\frac{T_{\text{hys}}(M_s)}{2} = T_{\text{ath}} + T_{\text{th}}(0) \left\{ 1 - \left( \frac{M_s}{T_{\text{TA}}} \right)^{1/q} \right\}^{1/p} \quad (2)$$

where  $T_{\text{hys}}$  replaces  $\sigma_{\text{hys}}$  and  $M_s$  replaces the testing temperature ( $T$ ) in equation (1).

$T_{\text{th}}$  and  $T_{\text{ath}}$  are analogous to  $\sigma_{\text{TA}}$  and  $\sigma_{\mu}$ , respectively. As mentioned before,  $T_{\text{hys}}$  of a thermoelastic MT is contributed by the athermal and thermal part [30].

Correspondingly,  $T_{\text{ath}}$  stands for the athermal part, and  $T_{\text{th}}(0)$  stands for the thermal part at 0K at which the thermal activation is zero. And the whole second term in equation (2) is the thermal contribution to  $T_{\text{hys}}$  (the value in the braces is less than 1).

As shown in Fig. 4, the experimental data from  $\text{Ni}_{50.5}\text{Ti}_{47.5}\text{Nb}_2$  specimens can be well fitted by equation (2) using  $p = 1/2$ ,  $q = 3/2$ ,  $T_{\text{ath}} = 21.6\text{K}$ ,  $T_{\text{th}}(0) = 218.5\text{K}$ , and  $T_{\text{TA}} = 300.9\text{K}$ . Note that  $T_{\text{th}}(0)$  is about one order of magnitude larger than  $T_{\text{ath}}$ , again indicating the major contribution of the thermal part. Furthermore, the  $p$  and  $q$  values used here are in very good agreement with those in literature [34,36,37], manifesting the existence of a strain coupling between phase boundary with obstacles (strain energy to be released). This modified kinetic model justifies the strong connection between kinetic resistance and  $T_{\text{hys}}$  in  $\text{Ni}_{50.5}\text{Ti}_{47.5}\text{Nb}_2$ . Therefore, the underlying physics of the large and grain-size-dependent  $T_{\text{hys}}$  can be finally established, that is, smaller grain size leads to enhanced kinetic resistance of MT which subsequently renders larger  $T_{\text{hys}}$ .

In summary, the thermally-induced MT behavior of a single-phase ( $\beta$ -Nb-free)  $\text{Ni}_{50.5}\text{Ti}_{47.5}\text{Nb}_2$  SMA has been investigated and compared with a  $\text{Ni}_{50}\text{Ti}_{50}$  alloy. It has been found that the single-phase  $\text{Ni}_{50.5}\text{Ti}_{47.5}\text{Nb}_2$  alloys obtain large intrinsic  $T_{\text{hys}}$  up to

100K, which is comparable to that of the commercial dual-phase NiTiNb alloys. The grain-size-dependence on  $T_{\text{hys}}$  in single-phase ( $\beta$ -Nb-free)  $\text{Ni}_{50.5}\text{Ti}_{47.5}\text{Nb}_2$  has been suggested to attribute to the enhanced kinetic resistance according to a modified dislocation-based kinetic model.

## Acknowledgments

K. Yu acknowledges financial support from the National Natural Science Foundation of China (NSFC 91963112 and 51871241). L. Cui acknowledges financial support from NSFC 51731010 and 51971243. The use of the Advanced Photon Source was supported by the US Department of Energy, Office of Science, and Office of Basic Energy Science under Contract no. DE-AC02-06CH11357.

## References

- [1] T.W. Duerig, K.N. Melton, J.L. Proft, in: T.W. Duerig, K.N. Melton, D. Stöckel, C.M. Wayman (Eds.), *Eng. Asp. Shape Mem. Alloy.*, Butterworth-Heinemann, 1990, pp. 130–136.
- [2] J. Wang, C. Jiang, *Scr. Mater.* 62 (2010) 298–300.
- [3] X. Zhao, X. Yan, Y. Yang, H. Xu, *Mater. Sci. Eng. A* 438 (2006) 575–578.
- [4] L.C. Zhao, T.W. Duerig, S. Justi, K.N. Melton, J.L. Proft, W. Yu, C.M. Wayman, *Scr. Metall. Mater.* 24 (1990) 221–225.
- [5] C.S. Zhang, L.C. Zhao, T.W. Duerig, C.M. Wayman, *Scr. Metall. Mater.* 24 (1990) 1807–1812.
- [6] M. Piao, K. Otsuka, S. Miyazaki, H. Horikawa, *Mater. Trans. JIM* 34 (1993) 919–929.
- [7] X. He, L. Rong, D. Yan, Z. Jiang, Y. Li, *Metall. Mater. Trans. A* 35 (2004) 2783–2788.
- [8] X.M. He, L.J. Rong, D.S. Yan, Y.Y. Li, *Mater. Sci. Eng. A* 371 (2004) 193–197.
- [9] K. Tsuchiya, Y. Hada, T. Koyano, K. Nakajima, M. Ohnuma, T. Koike, Y. Todaka, M. Umemoto, *Scr. Mater.* 60 (2009) 749–752.
- [10] C. Yu, B. Aoun, L. Cui, Y. Liu, H. Yang, X. Jiang, S. Cai, D. Jiang, Z. Liu, D.E. Brown, Y. Ren, *Acta Mater.* 115 (2016) 35–44.
- [11] X.B. Shi, F.M. Guo, J.S. Zhang, H.L. Ding, L.S. Cui, *J. Alloys Compd.* 688 (2016) 62–68.

- [12] T. Waitz, V. Kazykhanov, H.P. Karnthaler, *Acta Mater.* 52 (2004) 137–147.
- [13] T. Waitz, T. Antretter, F.D. Fischer, H.P. Karnthaler, *Mater. Sci. Technol.* 24 (2008) 934–940.
- [14] T. Waitz, T. Antretter, F.D. Fischer, N.K. Simha, H.P. Karnthaler, *J. Mech. Phys. Solids* 55 (2007) 419–444.
- [15] C.M. Hwang, M. Meichle, M.B. Salamon, C.M. Wayman, *Philos. Mag. A* 47 (1983) 9–30.
- [16] D. Shindo, Y. Murakami, T. Ohba, *MRS Bull.* 27 (2002) 121–127.
- [17] S. Sarkar, X. Ren, K. Otsuka, *Phys. Rev. Lett.* 95 (2005) 205702.
- [18] M.-S. Choi, T. Fukuda, T. Kakeshita, H. Mori, *Philos. Mag.* 86 (2006) 67–78.
- [19] D. Wang, Z. Zhang, J. Zhang, Y. Zhou, Y. Wang, X. Ding, Y. Wang, X. Ren, *Acta Mater.* 58 (2010) 6206–6215.
- [20] Z. Zhang, Y. Wang, D. Wang, Y. Zhou, K. Otsuka, X. Ren, *Phys. Rev. B* 81 (2010) 224102.
- [21] J. Frenzel, E.P. George, A. Dlouhy, C. Somsen, M.F.-X. Wagner, G. Eggeler, *Acta Mater.* 58 (2010) 3444–3458.
- [22] C.M. Hwang, C.M. Wayman, *Scr. Metall.* 17 (1983) 381–384.
- [23] I. Yoshida, D. Monma, T. Ono, *J. Alloys Compd.* 448 (2008) 349–354.
- [24] S.-H. Chang, C. Chien, S.-K. Wu, *Mater. Trans.* 57 (2016) 351–356.
- [25] M. Piao, S. Miyazaki, K. Otsuka, *Mater. Trans. JIM* 33 (1992) 346–353.
- [26] X.M. He, D.S. Yan, L.J. Rong, Y.Y. Li, in: *AIP Conf. Proc.*, American Institute of Physics, 2006, pp. 11–18.
- [27] X. Fu, Z. Xinqing, X. Huibin, J. Haichang, R. Lijian, *Acta Metall. Sin.* 45 (2009) 18–24.
- [28] H. Yin, G. Ma, Q. Fan, Y. Wang, S. Huang, Y. Yi, *Metals*. 9 (2019) 214.
- [29] M.A.R. Medeiros, C.J. de Araújo, *J. Alloys Compd.* 866 (2021) 158970.
- [30] E.L. Pang, G.B. Olson, C.A. Schuh, *Acta Mater.* 213 (2021) 116972.
- [31] J. Cui, Y.S. Chu, O.O. Famodu, Y. Furuya, J. Hattrick-Simpers, R.D. James, A. Ludwig, S. Thienhaus, M. Wuttig, Z. Zhang, I. Takeuchi, *Nat. Mater.* 5 (2006) 286–290.
- [32] R. Zarnetta, R. Takahashi, M.L. Young, A. Savan, Y. Furuya, S. Thienhaus, B. Maaß, M. Rahim, J. Frenzel, H. Brunken, Y.S. Chu, V. Srivastava, R.D. James, I. Takeuchi, G. Eggeler, A. Ludwig, *Adv. Funct. Mater.* 20 (2010) 1917–1923.
- [33] Y. Song, X. Chen, V. Dabade, T.W. Shield, R.D. James, *Nature* 502 (2013) 85–88.
- [34] K. Niitsu, T. Omori, R. Kainuma, *Appl. Phys. Lett.* 102 (2013) 231915.

- [35] K. Niitsu, H. Date, R. Kainuma, *Scr. Mater.* 186 (2020) 263–267.
- [36] Y. Kimura, X. Xu, K. Niitsu, T. Omori, R. Kainuma, *Mater. Trans.* 57 (2016) 269–277.
- [37] K. Niitsu, X. Xu, R.Y. Umetsu, R. Kainuma, *Appl. Phys. Lett.* 103 (2013) 242406.
- [38] J. Liu, M. Jin, C. Ni, Y. Shen, G. Fan, Z. Wang, Y. Zhang, C. Li, Z. Liu, X. Jin, *Phys. Rev. B* 84 (2011) 140102.
- [39] S. Kartha, J.A. Krumhansl, J.P. Sethna, L.K. Wickham, *Phys. Rev. B* 52 (1995) 803–822.
- [40] Y. Ni, A.G. Khachatryan, *Nat. Mater.* 8 (2009) 410–414.
- [41] Y.C. Xu, W.F. Rao, J.W.M. Jr., A.G. Khachatryan, *Npj Comput. Mater.* 4 (2018) 1–7.
- [42] H.C. Tong, C.M. Wayman, *Acta Metall.* 22 (1974) 887–896.
- [43] K. Niitsu, Y. Kimura, X. Xu, R. Kainuma, *Shape Mem. Superelasticity* 1 (2015) 124–131.
- [44] G.-Y. Liao, B. Chen, Q.-K. Meng, M.-J. Wang, X.-Q. Zhao, *Rare Met.* 34 (2015) 829–832.

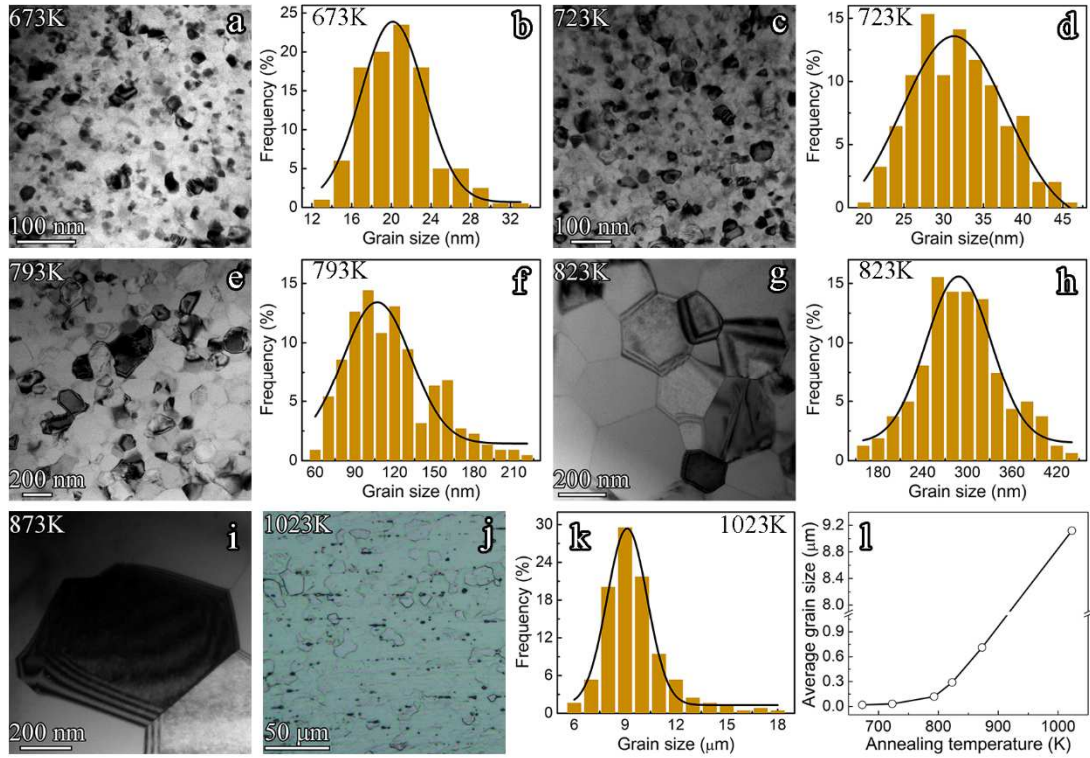


**Fig. 1.** Microstructure of the  $\text{Ni}_{50.5}\text{Ti}_{47.5}\text{Nb}_2$  alloy annealed at different temperatures. (a), (c), (e), (g), (i) Transmission electron microscopic (TEM) bright field images, and (j) optical microscopic (OM) image, of the alloy annealed at 673K, 723K, 793K, 823K, 873K and 1023K, respectively, showing equiaxial grains. (b), (d), (f), (h) and (k) Corresponding grain size statistics, showing average sizes of 20 nm, 31 nm, 110 nm, 290 nm and 9.1  $\mu\text{m}$ , respectively. (l) Average grain size as a function of annealing temperature.

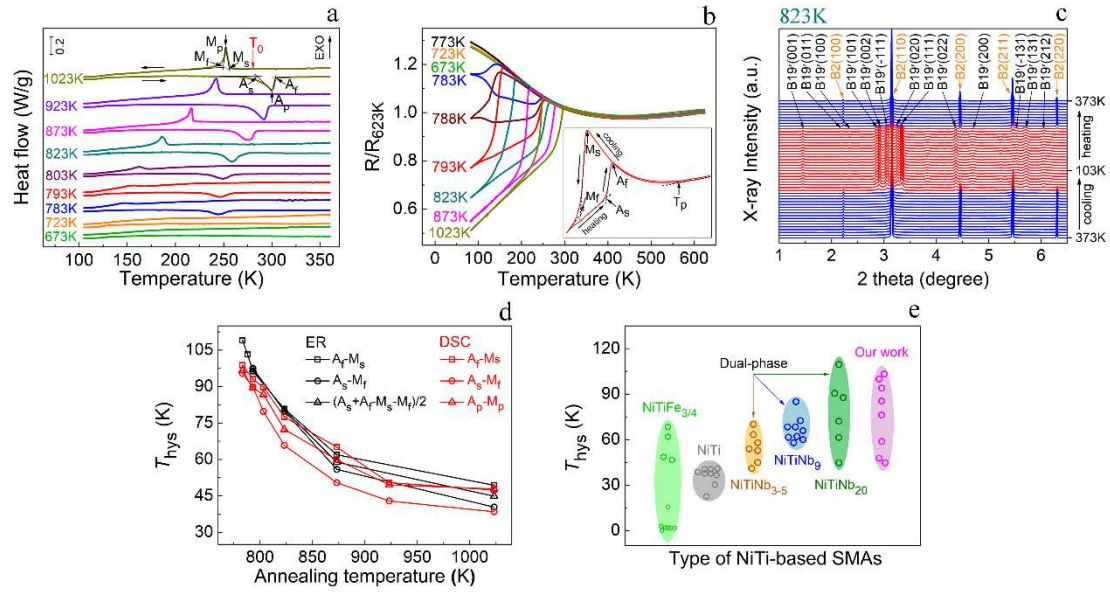


**Fig. 2.** Thermal transformation behavior of the  $\text{Ni}_{50.5}\text{Ti}_{47.5}\text{Nb}_2$  alloy annealed at different temperatures. (a) Differential scanning calorimeter (DSC) curves during cooling and heating within 105-360K. (b) Normalized electrical resistivity ( $R/R_{623\text{K}}$ ) curves during cooling and heating within 83-623K. (c) High-energy X-ray diffraction (HE-XRD) patterns of the alloy annealed at 823K during cooling and heating, showing reversible  $\text{B2} \leftrightarrow \text{B19}'$  martensitic transformation (MT). (d) Thermal hysteresis ( $T_{\text{hys}}$ ) as a function of annealing temperature. (e) Comparison of the intrinsic  $T_{\text{hys}}$  of various undeformed NiTi-based alloys.

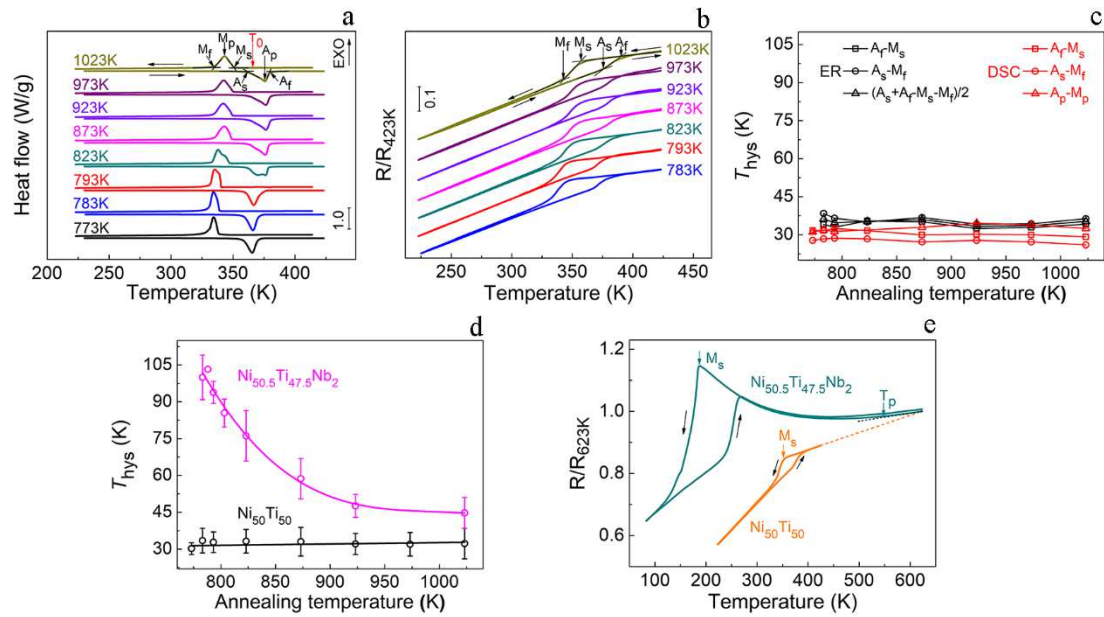


**Fig. 3.** Thermal transformation behavior of the Ni<sub>50</sub>Ti<sub>50</sub> alloy annealed at different temperatures. (a) DSC curves during cooling and heating within 223-423K. (b) Normalized electrical resistivity (R/R<sub>423K</sub>) curves during cooling and heating within 223-423K. (c) T<sub>hys</sub> as a function of annealing temperature. (d) Comparison of average T<sub>hys</sub> vs annealing temperature curves of Ni<sub>50.5</sub>Ti<sub>47.5</sub>Nb<sub>2</sub> and Ni<sub>50</sub>Ti<sub>50</sub>. (e) Comparison of the resistivity curves of Ni<sub>50.5</sub>Ti<sub>47.5</sub>Nb<sub>2</sub> and Ni<sub>50</sub>Ti<sub>50</sub> annealed at 823K.

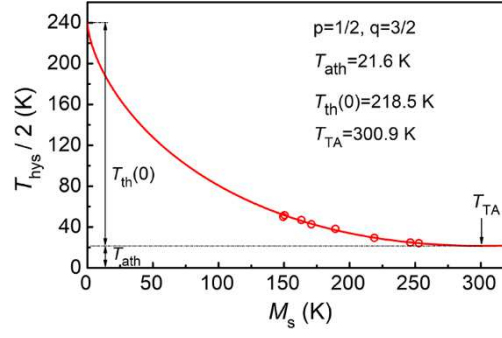


**Fig. 4.** Half of the average thermal hysteresis ( $T_{hys}/2$ ) as a function of  $M_s$  of the

$Ni_{50.5}Ti_{47.5}Nb_2$  alloy. Solid line is the fitting curve using  $\frac{T_{hys}(M_s)}{2} = T_{ath} +$

$$T_{th}(0) \left\{ 1 - \left( \frac{M_s}{T_{TA}} \right)^{1/q} \right\}^{1/p} .$$

